Generation of aperiodic motion due to sporadic collisions of camphor ribbons

Rishabh Jain [1], Jyoti Sharma,[2] Ishant Tiwari [2], Sangeeta D. Gadre,[1] Suresh Kumarasamy [3],
P. Parmananda,[2] and Awadhesh Prasad [4]

[1]*Kirori Mal College, University of Delhi, Delhi 110007, India*
[2]*Department of Physics, Indian Institute of Technology, Bombay, Powai, Mumbai, Maharashtra 400076, India*
[3]*Centre for Nonlinear Systems, Chennai Institute of Technology, Chennai 600069, India*
[4]*Department of Physics & Astrophysics, University of Delhi, Delhi 110007, India*

We present numerical and experimental results for the generation of aperiodic motion in coupled active rotators. The numerical analysis is presented for two point particles constrained to move on a unit circle under the Yukawa-like interaction. Simulations exhibit that the collision among the rotors results in chaotic motion of the rotating point particles. Furthermore, the numerical model predicts a route to chaotic motion. Subsequently, we explore the effect of separation between the rotors on their chaotic dynamics. The numerically calculated fraction of initial conditions which led to chaotic motion shed light on the observed effects. We reproduce a subset of the numerical observations with two self-propelled ribbons rotating at the air-water interface. A pinned camphor rotor moves at the interface due to the Marangoni forces generated by surface tension imbalance around it. The camphor layer present at the common water surface acts as chemical coupling between two ribbons. The separation distance of ribbons (L) determines the nature of coupled dynamics. Below a critical distance (L_T), rotors can potentially, by virtue of collisions, exhibit aperiodic oscillations characterized via a mixture of co- and counterrotating oscillations. These aperiodic dynamics qualitatively matched the chaotic motion observed in the numerical model.

I. INTRODUCTION

Exploring the dynamics of coupled nonlinear systems has been a focus of extensive research. Coupled nonlinear systems show a rich variety of nonlinear phenomena such as synchronization [1,2], chimera states [3], oscillation quenching [4,5], phase flips [6], traveling waves [7], etc. The collective dynamics of the coupled interacting oscillators have also been of considerable interest in various fields of science and engineering [8–10]. The resultant behavior of the coupled systems depends on the nature of coupling strength and coupling function between the systems. For example, the coupling between the oscillatory systems exhibiting synchronization can be mechanical in nature like a common support or spring [11,12], or chemical in nature as displayed by an oscillating Belousov-Zhabotinsky reaction [13], pentanol drops [14], and electrochemical cells [15]. Even electrical systems can manifest synchronized behavior, for example, in the brain [16], in power grids [1], and in electro-chemomechanical systems [17–21]. In the biological world, synchrony is exhibited in the flashing of fireflies and synchronization of circadian rhythms to day and night cycles [22]. There have also been a plethora of numerical demonstrations of coupled synchronized oscillations [23,24].

Studies have also shown that the sense of rotation, i.e., counterrotation (the opposite direction of rotation) of the oscillation, influences the resulting dynamics of the coupled oscillators. The counterrotating oscillators can induce mixed synchronization and amplitude death [25]. Moreover,

in the atmosphere and ocean dynamics, the counterrotating vortices are ubiquitous [26–28]. Furthermore, in the magnetohydrodynamics of plasma flow [29] and Bose-Einstein condensates [30] the counterrotating vortices are intentionally created for functional purposes. Counterrotating oscillation can induce traveling waves, bifurcation delay/preponement, and extreme events in a network of neurons [7,31]. Biological mediums such as protoplasm of the *Physarum plasmodium* also display counterrotating spirals [32]. All the above cases imply that counterrotating systems are omnipresent. Hence, their study is a pertinent problem. The corotating oscillators (same rotation direction) show in-phase synchronization. However, counterrotating oscillators show mixed synchronization, where a pair of state variables is in-phase synchronized while another pair of variables is antiphase synchronized. One can engineer a system that exhibits mixed synchronization [33]. However, the counterrotating oscillators spontaneously generate mixed synchronization.

Apart from rotation sense, the spatial separation between the oscillators plays a crucial role in their collective dynamics. The interaction strength among the oscillators depends on the Euclidean distance between them. Such systems can be found in a neurobiological setting of coupled neurons, the spatially embedded Kuramoto model [34–37], swarm aggregation of birds and fish [38], atomic interactions, and [39] micro air vehicles [40]. In real-time experiments, for example, in the synchronization of pendulums, spatial separation cannot be avoided. Moreover, a wide range of natural problems inherently have long-range interactions [41–43]. The omnipresence

of communication through spatial separation justifies the importance of a general and interdisciplinary understanding of such problems.

Based on the above facts, we study the dynamics of two coupled self-propelling camphor rotors in the current work. The choice of camphor rotors serves our motive to comprehend the coupled oscillators' dynamics via the rotational modes (corotating or counterrotating) and via the distance-dependent interactions. Using a table-top experimental setup and numerical tools, we will study the changes in the dynamics of co- and counteroscillating coupled systems when they are configured to collide with each other.

A camphor rotor (ribbon) is a camphor-infused rectangular paper strip. This camphor ribbon shows spontaneous motion at the air-water interface, i.e., translation or rotation. However, our interest here is to study the rotational dynamics of ribbons. Therefore, the ribbons are pinned at one of the ends to allow only rotation. A pinned ribbon touching the water surface rotates clockwise or anticlockwise. Self-rotation is generated by Marangoni forces acting on the rotor. This force arises due to surface tension imbalance induced by an inhomogeneously distributed camphor layer at the water surface [44]. In the case of two or more rotors placed at a common water surface, their camphor layers mutually interact with each other, which leads to chemical coupling between the rotors [45]. Under such spatial interaction, coupled camphor entities tend to show rich variety of collective dynamics, for instance, synchronization [46–49], chimera-like states [50], bursting dynamics [51], entrainment [52], and self-assembly [53]. Moreover, camphor particles have been explored in numerous experimental [54–57] and numerical [58] settings. A comprehensive review and developments related to the camphor system are provided in Ref. [57,59,60].

Furthermore, in a previous work [47], we simulated the coupled rotors dynamics via a numerical model, wherein two point particles interacted via the Yukawa potential. This model presents a bird's eye view of the experimental situation, but it was able to reproduce synchronization [46] and chimera-like states [50]. In the present study, this model is further explored. An exhaustive scan of state space and the parameter space provided a deeper insight into the coupled rotational dynamics of the simulated system from the nonlinear dynamics point of view.

The paper is organized as follows. Section II explains the (A) numerical model, (B) numerical results, and (C) analytical explanation of numerical results. Furthermore, II(B) is further divided into two subsections, wherein (1) chaotic collisions and (2) the route to the chaotic dynamics is discussed. In Sec. III we present an experimental verification of a subset of numerical inspections. This section details the (A) experimental setup followed by (B) the experimental results. Last, in Sec. IV we summarize the findings and discuss possible applications.

II. NUMERICS

A. Numerical model

We have considered the numerical model by Sharma *et al.* [47] involving two point particles (as shown in Fig. 1),
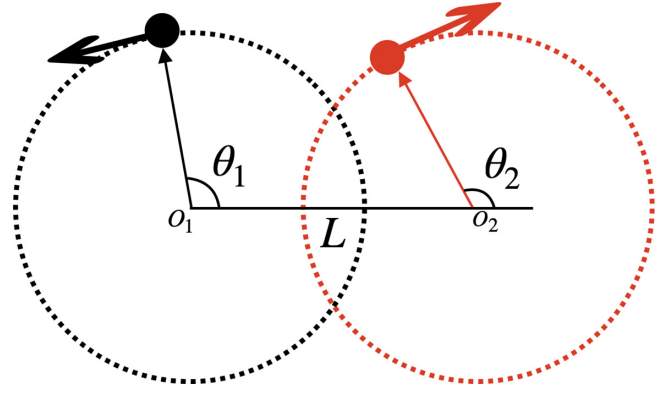

FIG. 1. Theoretical consideration of two point particles with unit mass, which are moving on a unit circle. O_1 and O_2 correspond to the pivots, and hence, L corresponds to the pivot-to-pivot distance between the ribbons in the experiments. This schematic figure is for the counterrotating case; however, the Hamiltonian in Eq. (9) remains the same for the corotating case as well.

each of unit mass, constrained to move on a unit circle. For the purpose of this work, we will refer to these point particles as a ribbon interchangeably since they are a numerical emulation of rotating ribbons in the experiments. It can be considered that the centers of the unit circles represent the pivot points for each ribbon in experiments. The pivots are kept at the origin $(0,0)$ and $(L,0)$. Therefore, the distance between the two pivots is L. The angular positions of the particles with respect to their constraining unit circle can be defined as $\theta_1(t)$ and $\theta_2(t)$, respectively. The positions of the particles with respect to the common origin in the Cartesian coordinate system are $\vec{r}_1(t) = (\cos\theta_1(t), \sin\theta_1(t))$ and $\vec{r}_2(t) = (L + \cos\theta_2(t), \sin\theta_2(t))$, respectively. When the two camphor rotors are placed at a common water surface, a repulsive force arises due to the camphor layer on the water surface. For the point particles simulated in the model, this repulsion can be represented through a repulsive Yukawa-type potential ($\frac{e^{-Kr}}{r}$) with a range determined by the scaling constant K. At any time t, for a radial distance $r(t) = |r_1(t) - r_2(t)|$ between the point particles, the Yukawa potential is $V_{Yukawa} = \frac{e^{-Kr(t)}}{r(t)}$. From the potential, the force between the two particles can be written as $\frac{e^{-Kr(t)}}{r(t)^2}[1 + Kr(t)]$, which determines the particle dynamics. The radial component of the Yukawa force is assumed to be balanced by the pivot constraint force. For finding the tangential component, we have

$$\vec{r}(t) = (\cos\theta_1 - \cos\theta_2 - L, \sin\theta_1 - \sin\theta_2), \quad (1)$$

$$r^2 = 2 + L^2 - 2L(\cos\theta_1 - \cos\theta_2) - 2\cos(\theta_1 - \theta_2), \quad (2)$$

$$\frac{\partial r}{\partial \theta_1} = \frac{1}{r}(L\sin\theta_1 + \sin(\theta_1 - \theta_2), \quad (3)$$

$$\frac{\partial r}{\partial \theta_2} = \frac{1}{r}(-L\sin\theta_2 + \sin(\theta_2 - \theta_1). \quad (4)$$

The Lagrangian of the system is given by

$$\mathcal{L} = T - V = \frac{1}{2}(\dot{\theta_1}^2 + \dot{\theta_2}^2) - V_Y(r). \quad (5)$$

The Hamiltonian is given by

$$H = \frac{1}{2}\left(\dot{\theta_1}^2 + \dot{\theta_2}^2\right) + \frac{e^{-Kr}}{r}. \quad (6)$$

From Eq. (6), the Hamiltonian of the two self-propelled camphor ribbons depends upon $\dot{\theta_1}^2$ and $\dot{\theta_2}^2$. Therefore for the same energy of the system, both $\dot{\theta_1}$ and $\dot{\theta_2}$ can be positive or negative. This results in the possibility of observing corotating (same sense of rotation) and counterrotating (opposite sense of rotation) camphor ribbons depending upon their initial states. A detailed calculation for the equations of motion of the rotator is given in the Appendix.

For numerical simulations, we use the RK4 method with a step size 10^{-3}. The dynamical measures are calculated for 10^6 iterations after discarding sufficient transients of 10^7 iterations. The parameter coefficient K is fixed at $K = 2$ throughout this work. We use the energy, E, and the pivot-to-pivot separation, L, as the tuneable parameters of the numerical system.

In the following section, we will discuss the various dynamics of two camphor ribbons and the influence of L on the dynamics.

B. Numerical results

In order to study the coupled behavior of the camphor ribbons, we consider Eqs. (A6) and (A7) with the fixed value $K = 2$. The variation of the spectrum of Lyapunov exponents (λ_i) [61] with the separation (L) between the two pivots is plotted in Fig. 2(a) for a fixed energy of $E = 20$ [62]. Here the sum of all the Lyapunov exponents (LEs) is zero ($\sum_{i=1}^4 \lambda_i = 0$), which confirms the conservation of energy for this system. For the parameter $L < L_T$ where $L_T \sim 2.7$ (written as L_T and defined in Sec. II B 2) the largest LEs for some of the initial conditions are positive, while for the remaining initial conditions, it is zero. This indicates that for $L < L_T$ both the chaotic and quasiperiodic motions are coexisting. The Poincaré sections for chaotic (scattered points) and quasiperiodic (points on a line) are shown in Figs. 2(b) and 2(c), respectively. The corresponding time series are shown in Figs. 2(d) and 2(e), respectively. The conservative nature of the system under study ensures that different initial conditions follow different trajectories. Hence, the period of oscillations may vary with different initial conditions; details are given in Fig. 4 below. For the region $L > L_T$, we find only quasiperiodic dynamics wherein the initial conditions determine the shape of the trajectories.

Trajectories in Figs. 2(d) and 2(e) show that one rotor has a higher frequency than the other. This behavior depends on the initial condition for a given energy. In other words, there is a possibility that the first rotor has a lower frequency than the second rotor or vice versa. This difference in frequency leads to an asynchronous state between the rotors and leads to chaotic motion. Moreover, just before the time $t \sim 4000$ [Fig. 2(d)], the second rotor shows a significant abrupt change. This behavior is, in fact, a type of collision, which is discussed in the following subsection.
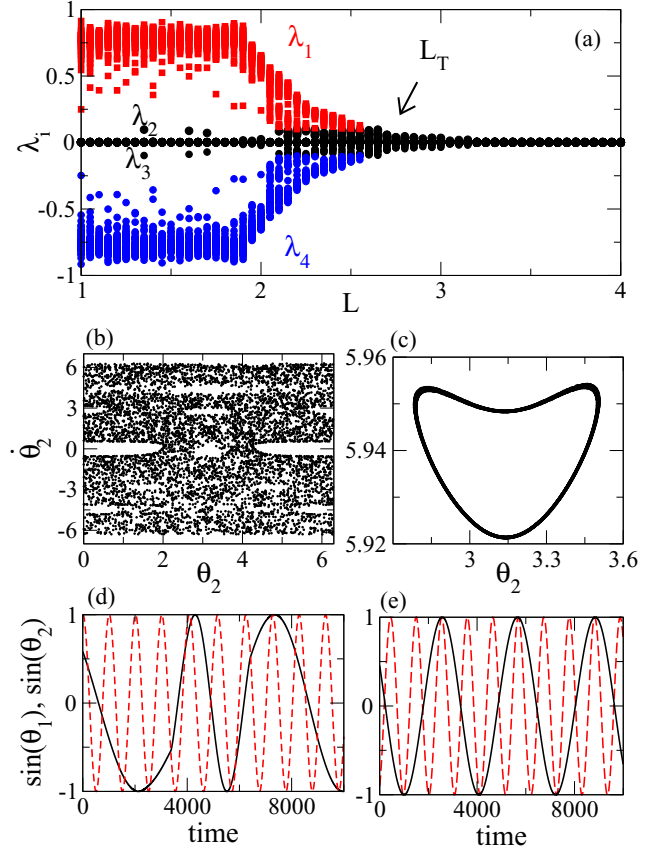

FIG. 2. (a) The variation of spectrum of Lyapunov exponents (λ_i) as a function of separation, L, between the two pivots. The Poincaré sections (taken at $\theta_1 = 0$) for (b) chaotic and (c) quasiperiodic motions at $L = 1.5$ with two different initial conditions ($\theta_1 = 2.4$, $\dot{\theta_1} = 2.7$, $\theta_2 = 0$, $\dot{\theta_2} = 5.72$) and ($\theta_1 = 1.02$, $\dot{\theta_1} = 2.03$, $\theta_2 = 0$, $\dot{\theta_2} = 6$), respectively. The time series of (b) and (c) are shown in (d) and (e), respectively. The solid (black) and dashed (red) lines correspond to the first and second rotors, respectively.

1. Chaotic motion: Collision of particles

The chaotic behavior of the rotor system for $L < L_T$ is the outcome of the collisions between them. We make our point using Fig. 3. A segment of the time series, θ_1 (dashed black line) and θ_2 (solid red line), of both the rotors is shown in Fig. 3(a). The second rotor shows significant changes at marked times, $C1$, $C3$, $C3$, $C4$, and $C5$. These points (in time) correspond to the collisions between the rotors. $C1$ and $C4$ indicate the points where collision changed the oscillators' direction, whereas $C2$, $C3$, and $C5$ are the points wherein the direction of rotation did not change. Note that a collision may also not change the mutual rotational state of the oscillators; for example, at collision point $C5$, the rotators remain corotating before and after the collision.

A proof of changes in velocities of the individual rotors corresponding to collision points $C3$ and $C4$ is shown in Fig. 3(b). At point $C3$, both $\dot{\theta_1}$ and $\dot{\theta_2}$ remain positive after the collision, meaning no flip in the rotational direction. It should be noted that before $C3$, particles are counterrotating, while after the collision, they exhibit a momentary change in the rotation direction (also observed experimentally) and
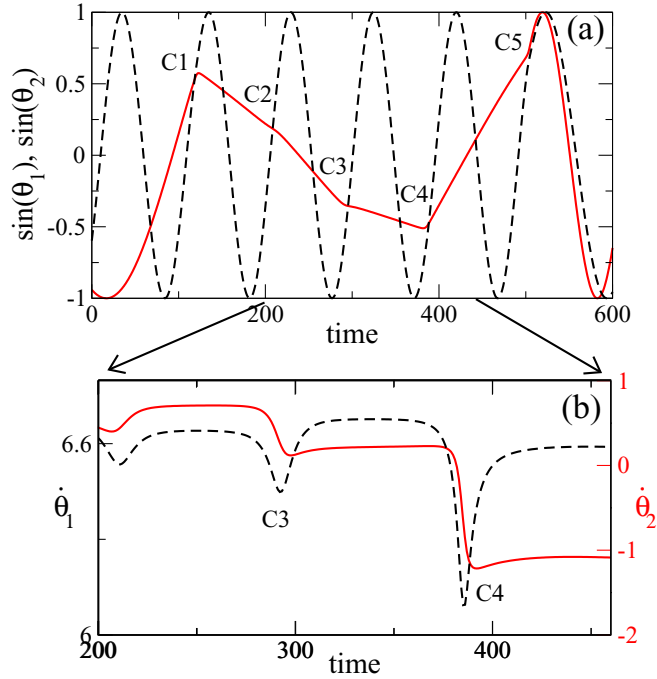
FIG. 3. The time series of (a) $\sin(\theta_1)$ and $\sin(\theta_2)$ and (b) $\dot\theta_1$ (left y axis) and $\dot\theta_2$ (right y axis) as a function of time of a chaotic motion with the initial conditions $\theta_1 = 3.31465984$, $\dot\theta_1 = 4.44012880$, $\theta_2 = 0$, $\dot\theta_2 = -5$ at $K = 2$ and $L = 1.5$. The collision points are indicated as $C1, C2, \ldots, C5$. The velocities of rotors near collision points, $C3$ and $C4$, are expanded in (b) where left and right y axes represent $\dot\theta_1$ and $\dot\theta_2$, respectively. The schematic illustration of collisions near $C3$ and $C4$ where counterrotating rotors remain counterrotating and counterrotating rotors become corotating are shown in (c) and (d), respectively. The dashed (black) and solid (red) lines correspond to the first and second rotors, respectively.

subsequently perform corotation. Finally, they maintain counterrotation as schematically illustrated in Fig. 3(c). However, at point $C4$, $\dot\theta_1$ (velocity) remains positive whereas $\dot\theta_2$ changes to negative, which implies a flip in the rotation direction of the second rotor. Therefore, in the vicinity of collision $C4$ countermoving rotors become comoving; refer to Fig. 3(b). In Fig. 3(b), the two particles' angular velocities are denoted by two different y axes. Hence, there can be changes in the velocity as well as the rotation direction of the rotors at collisions. The collisions of rotators collisions can be visualized in the Supplemental Material [63].

As discussed earlier, there are coexisting chaotic and quasiperiodic motions. No collisions were reported in quasiperiodic dynamics, even at the same energy E and separation L. It implies that the collision of rotors evokes chaotic motion. Moreover, we observed a few collision-like events beyond $L = 2$. However, the subset of initial conditions leading to chaotic motion starts decreasing, as explained in Sec. II B 2.

2. Route to chaos: Affinity for chaos as a function of rotator separation

Next, we explore the route to above mentioned chaotic dynamics. For this, we study the change in dynamics as a
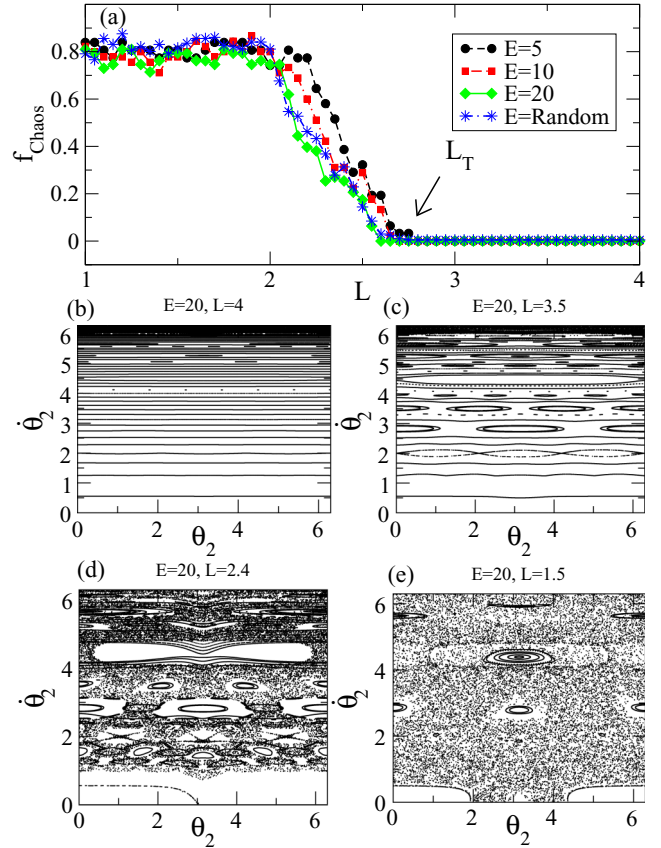

FIG. 4. (a) The fraction of initial conditions leading to chaotic motion (f_{chaos}) for different values of energy as a function of separation L. The Poincaré section for different trajectories corresponding to several initial conditions at different separations (b) $L = 4$, (c) $L = 3.5$, (d) $L = 2.4$, and (e) $L = 1.5$ at fixed energy $E = 20$. The generation of Poincaré sections in (b)–(e) is the same as that of Figs. 2(b) and 2(c).

function of separation parameter L. In Fig. 4(a) we present the fraction of initial conditions that led to chaotic motion from 200 randomly chosen initial conditions ($\theta_1 = \pi$, $\dot\theta_1 \in [-20, 20]$, $\theta_2 = 0$, $\dot\theta_2 = \sqrt{2[E - \frac{e^{-Kr}}{r}] - \dot\theta_1^2}$) for different energy levels $E = 5, 10$, and 20. For each E, 200 random initial conditions (ICs) were selected and simulated for a fixed L, and then the number of ICs leading to chaos is measured. Subsequently, the fraction of initial conditions leading to chaos is calculated, denoted by f_{chaos}. This process is repeated for various L values ($L = 1$ to $L = 4$). For the curve "$E = $ Random," the initial conditions are considered as ($\theta_1 = \pi$, $\dot\theta_1 \in [-20, 20]$, $\theta_2 = 0$, $\dot\theta_2 \in [-20, 20]$), i.e., each initial condition has different and random E. For a separation till $L = 2$, which is the total length of both the ribbons, f_{chaos} remains constant irrespective of the energies. As discussed in Sec. II B 1 collisions are more probable when the separation is below $L = 2$. Note that as L is further increased, f_{chaos} decreases linearly and vanishes at L_T after which we observe only quasiperiodic motion.

In order to understand the variation of f_{chaos}, we present the Poincaré section at different values of separation $L = 4, 3.5, 2.4$, and 1.5, but for fixed energy of $E = 20$, in
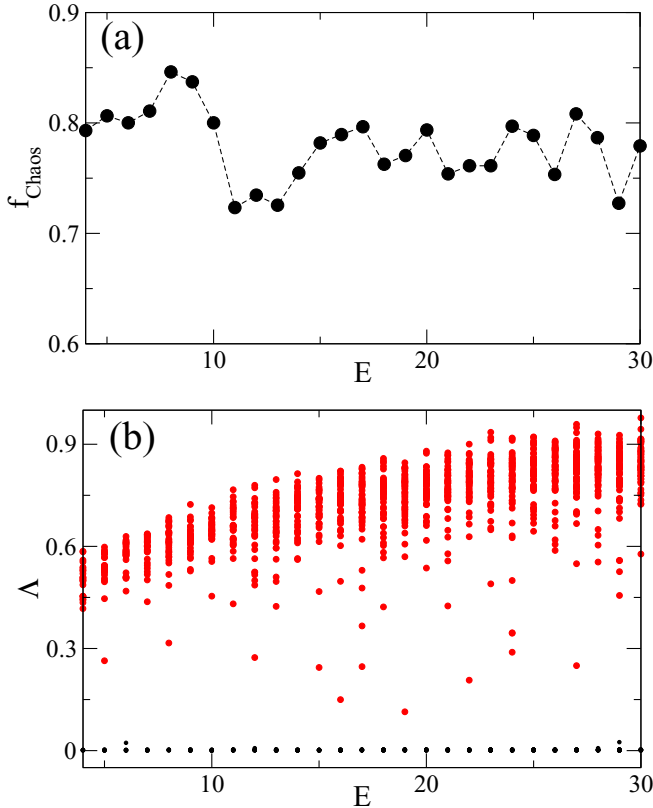
FIG. 5. The variation of (a) f_{chaos} and (b) the largest Lyapunov exponent as a function of the energy of the systems at $L = 1.5$.
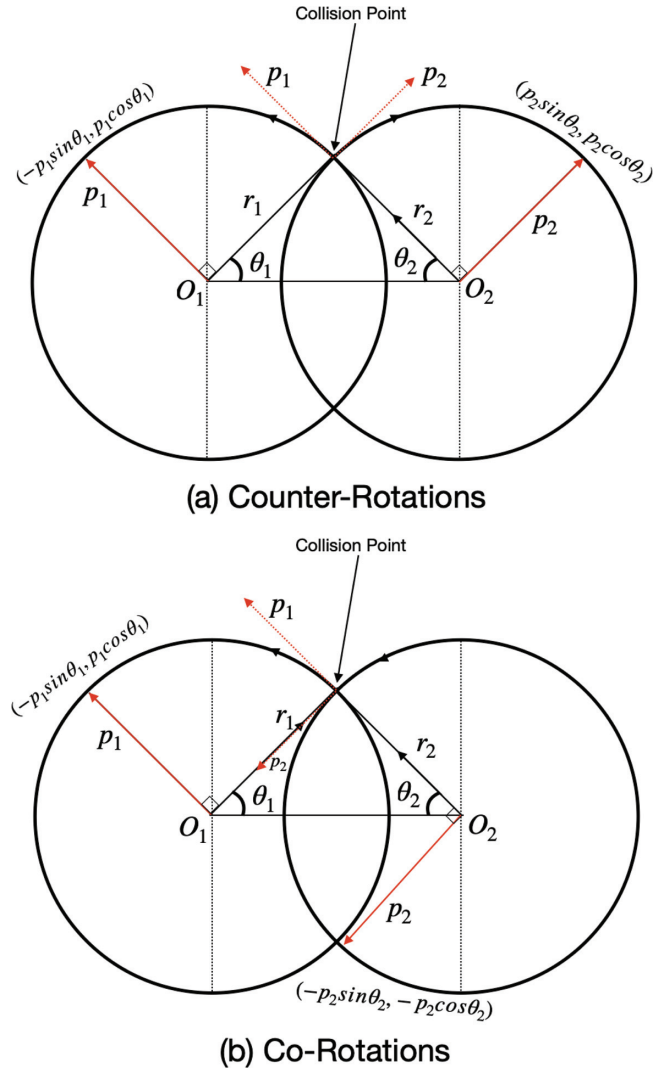

(a) Counter-Rotations

(b) Co-Rotations

FIG. 6. Schematic drawing of the collisions for (a) counterrotating and (b) corotating rotors. The dotted red lines represent the tangential momentum vectors of the rotors at the point of collision, and when shifted to respective centers of the circles, they are represented by solid red lines. The vectors r_1 and r_2 are radial vectors from the centers of respective circles to the point of collision represented by a solid black line. The arrows on circles represent the direction of rotation of each rotor. The rotors remain in counterrotation after collision in (a) while they change to corotations in (b).

Figs. 4(b), 4(c), 4(d), and 4(e), respectively. In each plot, trajectories of several initial conditions were considered. At $L = 4$ motions are quasiperiodic, and the curves are very smooth. As we decrease L further, the nested tori, i.e., small closed curves, start appearing. At $L = 2.4$, both the chaotic and quasiperiodic motions were observed. However, we mostly get chaotic motion for $L < 2$ because of a very high f_{chaos} and intermittent collisions. These transitions are a consequence of the KAM theorem [64]: as both the ribbons are far away, so they have weak interaction (perturbation to each other). However, when separation L is decreased, the interactions become stronger, and hence, the original torus decomposes into smaller and smaller tori. As per the KAM theorem, some of these tori are stable. However, irregular (chaotic) motion appears within the stable tori. Following the Poincaré-Birkhoff fixed point theorem, the rational tori break up and result in the appearance of chaotic seas [64,65].

Subsequently, we asked how the chaoticity of the system is affected as a function of energy. Therefore, in Figs. 5(a) and 5(b), we plot f_{chaos} and the largest Lyapunov exponents versus E for a fixed separation $L = 1.5$. Here Fig. 5(a) shows that f_{chaos} is almost constant, which is also evident in Fig. 4(a). However, the degree of chaoticity, in terms of the magnitude of the largest Lyapunov exponent, increases for some initial conditions. We argue that at higher energies, the ribbons may be colliding very frequently, thus, resulting in enhanced chaoticity for these ICs.

C. Analytical explanation

In this section, we will address collision dynamics analytically. Figure 6 mimics the geometrical possibilities of the rotors' directions before and after the collision. The red arrow in Fig. 6 represents the momentum vector of two rotors denoted by p_1 and p_2 (dashed arrows), while r_1 and r_2 are the position vectors of the rotors at the point of collision. The angles θ_1 and θ_2 are the deviations from the reference line $O_1 O_2$ (see Fig. 1). If the momentum vectors of both the rotors have opposite signs, it means they are exhibiting counterrotation [Fig. 6(a)], and if the signs are the same, then they are in corotation [Fig. 6(b)]. After a collision, a counterrotation (or corotation) of the two rotators can either remain in

counterrotation or become corotating. We understand it analytically by analyzing the conservation of momentum and energy before and after the collision [66].

Based on the conservation of momentum we have

$$-p_1 \sin\theta_1 + p_2 \sin\theta_2 = \pm p'_1 \sin\theta'_1 \pm p'_2 \sin\theta'_2, \quad (7)$$

where the prime symbol denotes the variables after the collision, and we have

$$p_1 \cos\theta_1 + p_2 \cos\theta_2 = \pm p'_1 \cos\theta'_1 \mp p'_2 \cos\theta'_2. \quad (8)$$

Also, from conservation of energy we have

$$\frac{p_1^2}{2m} + \frac{p_2^2}{2m} = \frac{p_1'^2}{2m} + \frac{p_2'^2}{2m}. \quad (9)$$

Squaring Eqs. (7) and (8), and adding them, we get

$$p_1^2 + p_2^2 + 2p_1 p_2(\beta) = p_1'^2 + p_2'^2 - 2p'_1 p'_2(\beta'),$$

where $\beta = (\cos\theta_1 \cos\theta_2 - \sin\theta_1 \sin\theta_2)$ and $\beta' = (\cos\theta'_1 \cos\theta'_2 - \sin\theta'_1 \sin\theta'_2)$. Now from Eq. (9), we have

$$\pm 2p_1 p_2 \cos(\theta_1 + \theta_2) = 2p'_1 p'_2 \cos(\theta'_1 + \theta'_2). \quad (10)$$

This equation helps in understanding the relationship between the relative momenta of the two rotors before and after collisions in the context of co- and counterrotation. We enumerate the various possibilities that arise from Eq. (10) below.

Case *i*: When we consider the negative (−) sign, then Eq. (10) becomes

$$-2p_1 p_2 \cos(\theta_1 + \theta_2) = 2p'_1 p'_2 \cos(\theta'_1 + \theta'_2). \quad (11)$$

This implies that rotors are in counterrotation before the collision (left-hand side of the equation). Since the $\cos(\theta_i)$ will always remain positive the momenta, p'_1 and p'_2 must have the same sign. This implies that one of the rotors changes its direction, and hence, both of the rotors have the same direction of rotations, i.e., corotation. It is evident in Fig. 3(b) that at collision point $C4$, the velocity of the second (red) rotor changes from positive to negative, resulting in rotation direction flip.

Case *ii*: However, if we consider positive (+) sign,

$$2p_1 p_2 \cos(\theta_1 + \theta_2) = 2p'_1 p'_2 \cos(\theta'_1 + \theta'_2), \quad (12)$$

which is possible only when the momenta, p'_1 or p'_2 has opposite signs. which implies that rotors remain counterrotating. This explains the collision point $C3$ in Fig. 3(b) where the velocities of rotors do not get changed in direction and both the ribbons remain in their previous directions of rotations even after the collision.

Similarly, we can have corotations before collision and counterrotation after collision, which corresponds to collision point $C1$ and corotation before and after collision as in the case of collision point $C5$ in Fig. 3(a).

III. EXPERIMENTS

In this section we describe an experimental setup which was used to realize a subset of the rich dynamics observed in numerics. Subsequently, the experimentally observed aperiodic dynamics of the rotors are presented.
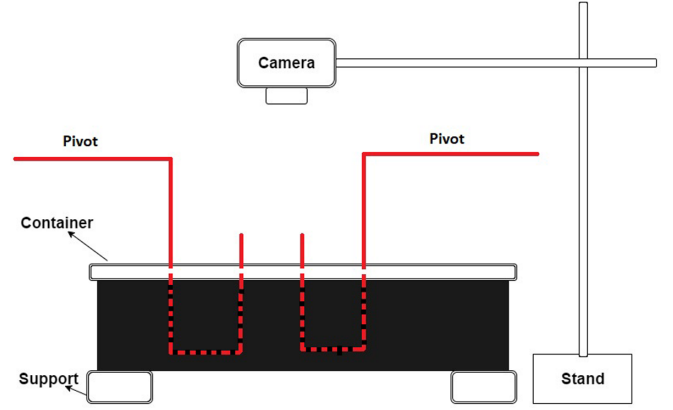

FIG. 7. Schematic of the experimental setup.

A. Experimental setup

The ribbons were prepared by cutting a rectangular piece of paper of dimensions 2.0 cm × 0.4 cm. Before cutting, their shape was already printed on an A4 size paper sheet. The template was such that the ribbon was black in color with a white circular region at one end to aid with the motion tracking of the ribbons. Following this, at room temperature, they were immersed in a 3.0 M camphor in ethanol solution for 60 s. The rectangular papers were air dried for 600 s. During this time, ethanol evaporated, and we were left with a paper ribbon infused with camphor in its matrix. This camphor-infused rectangular sheet will be called a camphor rotor or ribbon throughout this paper.

Subsequently, the ribbons were pivoted at one end using a thin wire (red wire in Fig. 7) and introduced to the surface of the water to observe their motion (Fig. 7). The ribbons were kept at a pivot-to-pivot distance ($L = 3.5$ cm), which is less than the span of the ribbons ($L_c = 4$ cm). At this distance, rotors will collide with each other if there is a frequency mismatch between them. Dynamics of the rotors were recorded with a high-speed GoPro camera set at 120 fps, 720 p. The experimental videos (see the Supplemental Material [63]) have been analyzed using the OpenCV library in the Python interface [67]. We track the white circular region at the distal end of each ribbon using this algorithm. For this work, we consider the position of the white circular region as a proxy for the position of the corresponding ribbon.

B. Experimental results

We observe that the aperiodic dynamics of the coupled rotators can be obtained at optimal pivot-to-pivot distances *L*. In Fig. 8 the time evolution of the *y* positions of the ribbon is plotted. Labels marked as E1, E2, and E3 represent the first, second, and third consecutive collisions between the rotors (see video 1.mp4 [63]). During collision E1, rotors do not switch their direction and remain corotating. However, in collision E2, the second rotor flips its direction (indicated by a transition of dashed red line to solid red line), and hence, rotors enter into a counterrotation regime. Last, while colliding for the third time (collision E3), the second rotor switches its direction (indicated by a transition of the solid line to the dashed line), leading to the corotation of the two rotors.
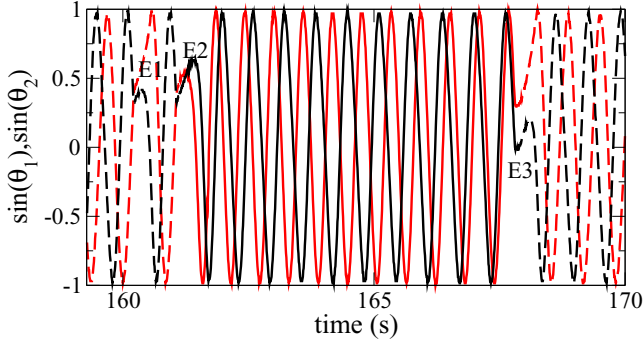
FIG. 8. Aperiodic dynamics of the rotators result from the sporadic collisions between them. The time series corresponds to the "y positions" of the rotors, i.e., the white regions present at each rotator's tips. The black and red lines correspond to the first and second rotors. E1, E2, and E3 represent the first, second, and third consecutive collisions between the rotors. The dashed lines correspond to a corotating pair, while the solid lines correspond to a counterrotating pair.

Hence, collisions E1$\rightarrow$ E2 $\rightarrow$ E3 result in a transition corotation $\rightarrow$ counterrotation $\rightarrow$ corotation dynamics. Note that the collisions in the experimental results are denoted as E, while the same is mentioned as C for numerical results in Fig. 3. Furthermore, it is evident from Fig. 8 that the ribbons exhibit aperiodic motion due to sporadic reversals in their rotation directions caused by collisions with the other ribbon [68]. This interesting phenomenon results from coupling (unsynchronization) between the rotors combined with being placed at a distance $L < L_T$ (physical collisions). We would emphasize that ribbons may not change their directions of rotation during each collision. Hence, a corotating (counterrotating) pair can remain corotating (counterrotating).

IV. SUMMARY

In this work, we numerically observed a rich dynamical behavior for repulsively interacting point particles. When the distance between the particles is more than the critical distance $L_T \sim 2.7$ the dynamics become quasiperiodic, whereas for a distance below the critical distance $L < L_T$, the coupled particles exhibited chaotic oscillation (collision) or coexistence of chaotic collision and quasiperiodic dynamics. Theoretical understanding of the two pinned self-propelled camphor ribbons was performed by two point particles with Yukawa interaction. All the possible dynamics of the rotators have been shown through numerical analysis. The collision of ribbons depending on the distance explains the reason for the quasiperiodic and chaotic motions. We used the conservation of energy and momentum arguments to shed light on the collisions of coupled ribbons analytically. Moreover, the coexistence of quasiperiodic and chaotic behavior was studied with Poincaré sections. The fraction of initial conditions leading to chaotic motion (f_{chaos}) calculations explained the effect of energy on the rise of chaotic behavior in coupled oscillators.

Moreover, we performed experiments with two ribbons rotating on the surface of the water, separated by a distance. We observed aperiodic motion, which is generated due to sporadic collisions of coupled camphor ribbons. The camphor ribbon placed a pivot to pivot distance L apart on the water surface interacts with each other due to the chemical coupling via the camphor layer. It needs to emphasized that although the numerical system explored in this work is conservative in nature, the experimental system explored in this study is a dissipative system. Therefore, we can reproduce only a subset of the dynamical aspects of the numerical observations such as aperiodic collisions between the two rotors.

The spatial separation is ubiquitous in natural systems. The present work gives a comprehensible understanding of how separation plays a role in determining the dynamics of coupled rotator ribbons. The results elucidate how chaotic dynamics occur in spatially separated self-propelled camphor rotor systems. This study can be utilized to understand systems like swarm aggregation, atomic interactions, micro air vehicles, etc. We believe that this work is a pertinent contribution in the field of active matter study from a nonlinear dynamics perspective. The rise of chaoticity in coupled rotational dynamics at the air-water interface will be of significant interest to active matter and the nonlinear dynamics community.

APPENDIX: EQUATIONS OF MOTION AND ENERGY CALCULATION

The radial component of the Yukawa force is assumed to be balanced by the pivot constraint force. For finding the tangential component, we have

$$\vec{r}(t) = (\cos\theta_1 - \cos\theta_2 - L, \sin\theta_1 - \sin\theta_2), \tag{A1}$$

$$\begin{aligned} r^2 = &\cos^2\theta_1 + \cos^2\theta_2 + L^2 - 2L\cos\theta_1 + 2L\cos\theta_2 \\ &- 2\cos\theta_1\cos\theta_2 + \sin^2\theta_1 + \sin^2\theta_2 \\ &- 2\sin\theta_1\sin\theta_2, \end{aligned} \tag{A2}$$

$$r^2 = 2 + L^2 - 2L(\cos\theta_1 - \cos\theta_2) - 2\cos(\theta_1 - \theta_2), \tag{A3}$$

$$\frac{\partial r}{\partial \theta_1} = \frac{1}{r}(L\sin\theta_1 + \sin(\theta_1 - \theta_2), \tag{A4}$$

$$\frac{\partial r}{\partial \theta_2} = \frac{1}{r}(-L\sin\theta_2 + \sin(\theta_2 - \theta_1). \tag{A5}$$

The Lagrangian of the system is given by

$$\mathcal{L} = T - V = \tfrac{1}{2}(\dot{\theta_1}^2 + \dot{\theta_2}^2) - V_Y(r).$$

Now, for the equation of motion the particle 1,

$$\frac{\partial \mathcal{L}}{\partial \dot{\theta_1}} = \dot{\theta_1} \quad \text{so} \quad \frac{\partial}{\partial t}\left(\frac{\partial \mathcal{L}}{\partial \dot{\theta_1}}\right) = \ddot{\theta_1},$$

$$\text{Also,} \quad \frac{\partial \mathcal{L}}{\partial \theta_1} = -\frac{\partial V}{\partial r}\frac{\partial r}{\partial \theta_1} = F_y \cdot \frac{\partial r}{\partial \theta_1}.$$

Putting this in an Euler-Lagrange framework gives

$$\ddot{\theta}_1 = \frac{e^{-Kr}}{r^3}(1 + Kr)(\sin(\theta_1 - \theta_2) + L\sin\theta_1) = (F_t)_1. \quad \text{(A6)}$$

Similarly for particle 2, the equation of motion can be obtained as

$$\frac{\partial \mathcal{L}}{\partial \dot{\theta}_2} = \dot{\theta}_2 \quad \text{so} \quad \frac{\partial}{\partial t}\left(\frac{\partial \mathcal{L}}{\partial \dot{\theta}_2}\right) = \ddot{\theta}_2$$

$$\text{and} \quad \frac{\partial \mathcal{L}}{\partial \theta_2} = -\frac{\partial V}{\partial r}\frac{\partial r}{\partial \theta_2} = F_y.\frac{\partial r}{\partial \theta_2}.$$

Putting this in an Euler-Lagrange gives

$$\ddot{\theta}_2 = \frac{e^{-Kr}}{r^3}(1 + Kr)[\sin(\theta_2 - \theta_1) - L\sin\theta_2] = (F_t)_2. \quad \text{(A7)}$$

The Hamiltonian is given by

$$H = \sum_i \frac{\partial L}{\partial \theta_i}\theta_i - \mathcal{L},$$

$$H = \left(\dot{\theta}_1^2 + \dot{\theta}_2^2\right) - \frac{1}{2}\left(\dot{\theta}_1^2 + \dot{\theta}_2^2\right) + \frac{e^{-Kr}}{r}, \quad \text{(A8)}$$

$$H = \frac{1}{2}\left(\dot{\theta}_1^2 + \dot{\theta}_2^2\right) + \frac{e^{-Kr}}{r}. \quad \text{(A9)}$$

Equation (A9) is used to calculate the Hamiltonian of the two self-propelled camphor ribbons. As we discussed earlier the Hamiltonian depends upon $\dot{\theta}_1^2$ and $\dot{\theta}_2^2$; therefore for the given energy, both $\dot{\theta}_1$ and $\dot{\theta}_2$ can be positive or negative.

[1] A. Pikovsky, M. Rosenblum, and J. Kurths, Cambridge Nonlinear Science Series 12, *Synchronization: A Universal Concept in Nonlinear Science* (Cambridge University Press, Cambridge, 2003), Vol. 12.

[2] Y. Kuramoto, *Chemical Oscillations, Waves and Turbulence* (Springer-Verlag, Berlin, 1984).

[3] M. J. Panaggio and D. M. Abrams, Nonlinearity **28**, R67 (2015).

[4] G. Saxena, A. Prasad, and R. Ramaswamy, Phys. Rep. **521**, 205 (2012)

[5] A. Koseska, E. Volkov, and J. Kurths, Phys. Rep. **531**, 173 (2013).

[6] A. Prasad, J. Kurths, S. K. Dana, and R. Ramaswamy, Phys. Rev. E **74**, 035204(R) (2006).

[7] V. Varshney, K. Suresh, A. Mishra, B. Biswal, and A. Prasad, Chaos **31**, 093136 (2021).

[8] S. H. Strogatz, *Nonlinear Dynamics and Chaos, with Applications to Physics, Biology, Chemistry, and Engineering* (Perseus Books, New York, 1994).

[9] A. T. Winfree, J. Theor. Biol. **16**, 15 (1967).

[10] S. H. Strogatz, *Sync: The Emerging Science of Spontaneous Order* (Hyperion Press, New York, 2003).

[11] K. Czolczynski, P. Perlikowski, A. Stefanski, and T. Kapitaniak, Commun. Nonlinear Sci. Numer. Simulat. **17**, 3658 (2012).

[12] N. Chakrabarty, A. Jain, N. Lal, K. Das Gupta, and P. Parmananda, Chaos **27**, 013115 (2017).

[13] R. Toth, A. F. Taylor, and M. R. Tinsley, J. Phys. Chem. B **110**, 10170 (2006).

[14] T. Roy, S. S. Chaurasia, J.-M. Cruz, V. Pimienta, and P. Parmananda, Soft Matter **18**, 1688 (2022).

[15] J. M. Cruz, M. Rivera, and P. Parmananda, Phys. Rev. E **75**, 035201(R) (2007).

[16] R. Phogat and P. Parmananda, Chaos **28**, 121105 (2018).

[17] A. Biswas, P. Kumar, D. Das, and P. Parmananda, Phys. Rev. E **99**, 032223 (2019).

[18] P. Kumar, D. K. Verma, P. Parmananda, and S. Boccaletti, Phys. Rev. E **91**, 062909 (2015).

[19] D. K. Verma, H. Singh, A. Q. Contractor, and P. Parmananda, J. Phys. Chem. A **118**, 4647 (2014).

[20] D. K. Verma, H. Singh, P. Parmananda, A. Q. Contractor, and M. Rivera, Chaos **25**, 064609 (2015).

[21] D. K. Verma, A. Q. Contractor, and P. Parmananda, J. Phys. Chem. A **117**, 267 (2013).

[22] S. Strogatz, *Sync: The Emerging Science of Spontaneous Order* (Penguin UK, London, 2004).

[23] Y. Jiang and P. Parmananda, Phys. Rev. E **57**, 4135 (1998).

[24] B. K. Bera, D. Ghosh, P. Parmananda, G. V. Osipov, and S. K. Dana, Chaos **27**, 073108 (2017).

[25] A. Prasad, Chaos Solitons Fractals **43**, 42 (2010).

[26] Y. Murakami and H. Fukuta, Fluid Dyn. Res. **31**, 1 (2002).

[27] H. Fukuta and Y. Murakami, Phys. Rev. E **57**, 449 (1998).

[28] P. Meunier and T. Leweke, J. Fluid Mech. **533**, 125 (2005).

[29] G. N. Throumoulopoulos and H. Tasso, Phys. Plasmas **17**, 032508 (2010).

[30] S. Thanvanthri, K. T. Kapale, and J. P. Dowling, J. Mod. Opt. **59**, 1180 (2012).

[31] V. Varshney, K. Suresh, B. Biswal, and A. Prasad, Eur. Phys. J.: Spec. Top. **229**, 2307 (2020).

[32] S. Takagi and T. Ueda, Physica D **237**, 420 (2008).

[33] I. Grosu, E. Padmanaban, P. K. Roy, and S. K. Dana, Phys. Rev. Lett. **100**, 234102 (2008).

[34] H. Mangesius, S. Hirche, and D. Obradovic, in *2012 American Control Conference (ACC)* (2012), p. 2159.

[35] S. Kumarasamy, S. Sabarathinam, P. B. Gogoi, and A. Prasad, Commun. Nonlinear Sci. Numer. Simulat. **107**, 106170 (2022).

[36] M. Breakspear, S. Heitmann, and A. Daffertshofer, Front. Human Neurosci. **4**, 190 (2010).

[37] J. Cabral, E. Hugues, O. Sporns, G. Deco, NeuroImage **57**, 130 (2011).

[38] V. Gazi, K. M. Passino, Int. J. Control **77**, 1567 (2004).

[39] A. Stone, *The Theory of Intermolecular Forces* (Oxford University Press, Oxford, 2016).

[40] M. Coppola, J. Guo, E. Gill, and G. C. de Croon, Swarm Intell. **13**, 59 (2019).

[41] M. E. Fisher, S. K. Ma, and B. G. Nickel, Phys. Rev. Lett. **29**, 917 (1972).

[42] A. Campa, T. Dauxois, and S. Ruffo, Phys. Rep. **480**, 57 (2009).

[43] H. Christiansen, S. Majumder, and W. Janke, Phys. Rev. E **99**, 011301(R) (2019).

[44] G. Van der Mensbrugghe, Mém. Courronnés l'Acad. Roy. Sci. Belg. **34**, 1 (1869).

[45] S. Nakata, Y. Iguchi, S. Ose, M. Kuboyama, T. Ishii, and K. Yoshikawa, Langmuir **13**, 4454 (1997).

[46] J. Sharma, I. Tiwari, D. Das, P. Parmananda, and V. Pimienta, Phys. Rev. E **101**, 052202 (2020).

[47] J. Sharma, I. Tiwari, D. Das, P. Parmananda, V. S. Akella, and V. Pimienta, Phys. Rev. E **99**, 012204 (2019).

[48] S. Nakata, Y. Doi, and H. Kitahata, J. Phys. Chem. B **109**, 1798 (2005).

[49] I. Tiwari, P. Parmananda, and R. Chelakkot, Soft Matter **16**, 10334 (2020).

[50] J. Sharma, I. Tiwari, D. Das, and P. Parmananda, Phys. Rev. E **103**, 012214 (2021).

[51] I. Tiwari, S. Upadhye, V. S. Akella, and P. Parmananda, Soft Matter **17**, 2865 (2021).

[52] J. Sharma, I. Tiwari, P. Parmananda, and M. Rivera, Phys. Rev. E **105**, 014216 (2022).

[53] H. Nishimori, N. J. Suematsu, and S. Nakata, J. Phys. Soc. Jpn. **86**, 101012 (2017).

[54] A. Biswas, J. M. Cruz, P. Parmananda, and D. Das, Soft Matter **16**, 6138 (2020).

[55] S. Nakata and S. Hiromatsu, Colloids Surf. A **224**, 157 (2003).

[56] N. J. Suematsu, T. Sasaki, S. Nakata, and H. Kitahata, Langmuir **30**, 8101 (2014).

[57] C. Tomlinson, London, Edinburgh, Dublin Philos. Mag. J. Sci. **38**, 409 (1869).

[58] M. Nagayama, S. Nakata, Y. Doi, and Y. Hayashima, Physica D **194**, 151 (2004).

[59] S. Nakata, M. Nagayama, H. Kitahata, N. J. Suematsu, and T. Hasegawa, Phys. Chem. Chem. Phys. **17**, 10326 (2015).

[60] V. Pimienta and C. Antoine, Curr. Opinion Colloid Interface Sci. **19**, 290 (2014).

[61] G. Benettin, L. Galgani, A. Giorgilli, and J.-M. Strelcyn, Meccanica **15**, 9 (1980).

[62] For generating the Fig. 2(a) we consider 200 initial conditions at each parameter L: for each initial condition we fixed the values of $\theta_1 = \pi$ and $\theta_2 = 0$ while $\dot{\theta}_2$ is calculated for each value of $\dot{\theta}_1 \in [-20, 20]$ from Eq. (6).

[63] See Supplemental Material at http://link.aps.org/supplemental/10.1103/PhysRevE.106.024201 for numerical and experimental videos.

[64] M. Tabor, *Chaos and Integrability in Nonlinear Dynamics: An Introduction* (Wiley-Interscience, New York, 1989).

[65] H. G. Schuster, *Deterministic Chaos: An Introduction* (Wiley-VCH, Weinheim, 1995).

[66] In Fig. 6 we can consider, say, Θ_2, as a deviation from a positive x axis. In this case a deviation will be $\theta_2 = \pi - \Theta_2$; however, the explanation of the collision dynamics remains the same.

[67] G. Bradski, The OpenCV Library, Dr. Dobb's Journal of Software Tools (2000).

[68] In experiment, the rotors slow down and eventually stop after a long time (more than 35 minutes) [47]. Since aperiodic motion was found for substantial duration of time, these are thus not a transient phenomenon.